

Additive Manufacturing of Li-Ion Batteries: A Comparative Study between Electrode Fabrication Processes

Sergio Pinilla,* Seán Ryan, Lorcan McKeon, Meiyang Lian, Sebastien Vaesen, Ahin Roy, Wolfgang Schmitt, Jonathan N. Coleman, and Valeria Nicolosi*

Additive manufacturing strategies are gaining more importance in the context of lithium-ion batteries. The rapid prototyping, reduced waste and complex 3D structures achievable are powerful and attractive tools that are out of the reach of current fabrication techniques. Additionally, thanks to the potential that these manufacturing techniques hold for the fabrication of micro-energy storage devices, they are gaining increasing attention in the literature. Here, some of the more common additive manufacturing techniques are compared to standard methodologies by systematically evaluating their electrochemical performance and correlating it with the physical changes induced by the printing process. By using LTO/CNT-based inks, it is observed that the inner arrangement of the conductive additive is significantly altered depending on the technique used and that this has an impact on the rate performance of the device. By using a model that links the capacity-rate data to the physical properties of the batteries, it is possible to find the limiting factor on the printed electrodes and correlate it with the material arrangement that each technique produces.

the energy storage field, including the lithium-ion battery industry. With the rising popularity of solid-state batteries, many have seen additive manufacturing as the future of the industry, due to the flexibility of design, reduced waste, the complex designs achievable that boost power and energy densities and reduced use of casing and current collectors.^[3] In fact, we can already see some examples of companies that are walking down the path of 3D printing for lithium-ion batteries, including Photocentric, Sakuú and Blackstone Technology GmbH; with the last two planning to deliver prototypes in early 2023 and 2025 respectively.^[4,5]


Although the field has advanced rapidly, the youth of the field is still present in the optimization level of the functional inks aimed at specific printing methodologies. This comes accentuated by the fact that different techniques have different chal-

lenges associated, and multi-material/composite inks, which are of common use in batteries, require even more careful design and optimization.^[6] These issues commonly result in the end devices as brittleness, higher resistivities and reduced electrochemical performances.^[7] It is therefore fundamental in the development of this technology, to clearly narrow the origin of the issues and propose specific strategies for their solution or mitigation. With this objective in mind, our work aims to study some of the most common additive manufacturing techniques and, employing a novel methodology, quantify the

1. Introduction

In the last few years, we have witnessed a very fast development of the additive manufacturing industry. Since the patenting of fused deposition modelling (FDM) in 1992, 3D printing has evolved massively through the creation of new techniques, printable materials, and better accuracies.^[1] Additive manufacturing now is present in all markets with an estimated value of USD 18 billion in 2022 and this value is expected to reach 84 billion in 2029.^[2] The market penetration is also reaching

S. Pinilla, S. Ryan, L. McKeon, M. Lian, S. Vaesen, A. Roy, W. Schmitt, J. N. Coleman, V. Nicolosi
Centre for Research on Adaptive Nanostructures and Nanodevices (CRANN) and Advanced Materials
Bio-Engineering Research Centre (AMBER)
Trinity College Dublin
Dublin 2 D02 W9K7, Ireland
E-mail: sergio.pinilla@imdea.org; nicolov@tcd.ie

 The ORCID identification number(s) for the author(s) of this article can be found under <https://doi.org/10.1002/aenm.202203747>.

© 2023 The Authors. Advanced Energy Materials published by Wiley-VCH GmbH. This is an open access article under the terms of the Creative Commons Attribution License, which permits use, distribution and reproduction in any medium, provided the original work is properly cited.

DOI: 10.1002/aenm.202203747

S. Pinilla, S. Ryan, L. McKeon, M. Lian, S. Vaesen, A. Roy, W. Schmitt, J. N. Coleman, V. Nicolosi
School of Chemistry
Trinity College Dublin
Dublin 2 D02 W9K7, Ireland
S. Pinilla
Electrochemical Processes Unit
IMDEA Energy
Avda. Ramón de la Sagra 3, Móstoles, Madrid 28935, Spain
A. Roy
Materials Science Centre
Indian Institute of Technology Kharagpur
Kharagpur 721302, India
J. N. Coleman
School of Physics
Trinity College Dublin
Dublin 2 D02 K8N4, Ireland

performance loss and its origin. We used as electrode material a composite based on $\text{Li}_4\text{Ti}_5\text{O}_{12}$ (LTO) and single-wall carbon nanotubes (CNTs). CNTs, in combination with micro-sized active material particles, have been demonstrated to produce segregated networks that significantly improve the mechanical and electrochemical properties due to their binding effect.^[8] These properties are very desirable in printed devices, as some rely on high aspect ratio structures, and the deep integration of these materials in the battery industry makes them the ideal subject for the investigation of the changes that the 3D printing techniques induce in the final structure. To study these changes and their implications, we focused on the analysis of the microstructure and the rate performance of the electrodes. Rate performance is heavily influenced by the physical parameters of the electrodes, and recently, models have been developed correlating the time constants associated with the charge–discharge of the devices, with the physical magnitudes that limit them.^[9,10] This conforms the perfect toolbox for our studies, as it gives us the whole picture. We can observe how the microstructure of the electrodes changes with the fabrication technique, what impact that has on the rate performance, and finally, we can correlate the limitations with changes in specific magnitudes (i.e., porosity, conductivity, ion diffusivity, etc.). Hence, it allows for a very sharp optimization process for both inks and printing processes.

2. Results and Discussion

2.1. Material Preparation

To investigate how the deposition technique influences the material arrangement and its consequences on the performance as electrode material, we selected LTO as the active material for all the tests conducted in this work. LTO was combined with CNTs which fulfilled the role of binder and conductive additive.^[11] CNTs combine excellent conductivity, mechanical robustness, and typically require a much lower mass fraction (M_F) than other additives, which boosts the capacity of the electrodes. For instance, Park et al.^[8] found that CNT M_F as low as 2% outperformed the standard 20% PAA/CB combination, in electrical, electrochemical, and mechanical properties. Using active materials with higher particle size, this M_F could be further reduced to 0.5% in the case of lithium nickel manganese cobalt oxide (NMC).

To track how the deposition techniques affect the performance of the materials at different M_F , three percentages (2.5%, 5%, and 10%) were selected that were well above the percolation threshold (Figure S1, Supporting Information). All

deposition techniques were fed from the same masterbatches, reducing the potential inconsistencies that may be introduced through experimental errors. These slurries were prepared with $\approx 5\%$ of solid content and only in the case of the spray and aerosol jet printing these solutions were further diluted with DI water. The quality of the active material was checked throughout all the steps of the fabrication process by x-ray diffraction (XRD) (Figure S2, Supporting Information) and no change could be observed in the crystallographic structure from the starting powder to the electrode placed in the cell.

2.2. Microstructure and Material Arrangement

When CNTs are combined with the active material, the inner arrangement of the composite has deep implications for the performance of the electrodes. There are two possible distributions of the CNTs in the composites. The first one is a homogeneous distribution of CNTs along the thickness of the electrode^[12] and the second one, is a segregated network of CNTs.^[8] Generally speaking, the change from one type of arrangement to the other is catalyzed by the size of the particles accompanying the CNTs. For nanometric-sized particles, nanotubes distribute homogeneously across the electrode, while for micrometric-sized materials, segregated networks are formed.^[8] While this is true for common slurry casting techniques, to date, it is unknown if the formation of segregated networks is possible by other deposition techniques. The common advantages of the segregated networks are improved conductivity and the potential to fabricate thicker electrodes with higher robustness. These advantages are desirable not only in the context of high throughput techniques but also for new approaches such as additive manufacturing/printed devices where the aspect ratio is much higher than in common planar devices.^[13]

The distribution and arrangement of the material were studied for the five techniques; slurry casting, vacuum filtration, extrusion printing,^[14] spray coating,^[15] and aerosol jet printing,^[16] with different CNT M_F . For slurry casting samples (Figure S3, Supporting Information), it can be observed the formation of the segregated networks even at low CNT content. With the increase of the CNT percentage, more networks appear across the electrode thickness until reaching a maximum at moderate percentages (around 4%). Further increase in the CNT percentage seems to thicken the networks rather than form new ones (percentages of 7.5% and 10%).^[8] Other techniques such as extrusion printing and filtration follow the same trend with very similar network thickness and distribution for the different percentages (Figure S4, Supporting Information and Figure 1). However, techniques such as spray and

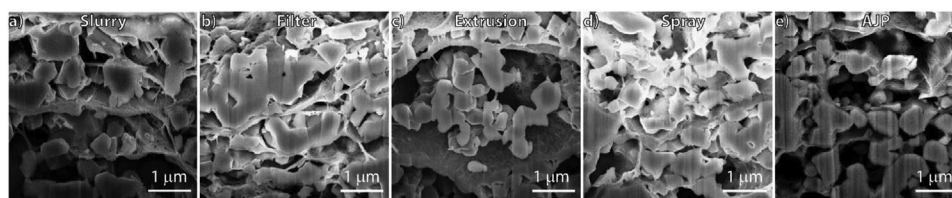


Figure 1. FIB-SEM cross-sections of electrodes obtained by a) slurry, b) filtration, c) extrusion, d) spray coating, and e) AJP. All were prepared using the same CNT mass fraction, i.e., 5%.

aerosol jet printing (AJP) show substantial differences from the slurry samples. Although Spray samples still display the presence of segregated networks (Figure S4, Supporting Information), they are much thinner than those created by other techniques (Figure 1d). Additionally, the increase of the CNT% does not have a major effect on the thickness of these networks and only further increases their presence across the width of the electrodes (at the percentages studied).

On the other side, AJP samples do not produce segregated networks at low to medium CNT percentages (Figure S4, Supporting Information), and only at high CNT percentages, some observable continuous networks are obtained.

The different behavior of the techniques can be attributed to the drying process of the inks during the deposition. By slurry and filtration, the CNTs have enough time to entangle and form the networks while the solvent is drying. Similarly, the extruded samples have layers thick enough (nozzle size of 0.40 mm) to reproduce this effect. On the other side, we have the extreme case of the AJP, where the deposited layers are very thin and the droplets of composite reach the material with a very limited volume of solvent, which does not allow the rearrangement of the CNT to form networks. These differences are illustrated in Figure S5 (Supporting Information), where it can be observed how a drop cast solution of LTO/CNT forms a network of thick channels, while AJP samples show a thinner and much more diffuse layer of CNTs. Spray coating is situated in the middle between these approaches, the inks are not dry when they reach the surface, but they are applied in such thin layers that when the next layer is applied, the previous one is fully dried, limiting the rearrangement of the CNT network. The differences in the drying processes are illustrated in **Scheme 1**.

Taking this into account, we can catalogue the deposition techniques in two broad groups that relate to the way the material reaches the substrate. These groups are “wet” and “dry” techniques. We will consider slurry casting, filtration and extrusion printing, wet techniques, while AJP and spray, dry techniques. Strictly speaking, spray coating does not fit perfectly in any of those categories, but somewhere in the middle; however, we will consider it a dry technique due to the limited rearrangement capability of the material.

2.3. Electrochemical Performance

Through the morphological characterization, it could be observed that the deposition technique mainly changes the arrangement of the filler (CNTs in our case) in the electrode. However, other physical parameters of the electrode are also altered when the deposition technique is changed. For instance, it could be observed that the roughness and porosity of the material deposited by dry techniques are higher than that of the wet, Figure S6 (Supporting Information). It has been recently shown by Tian et al. that the capacity-rate curves obtained by galvanostatic cycling (GC) and/or chronoamperometry (CA)^[17] can be linked to the physical parameters of the electrodes through a semiempirical model.^[10] In this section, we will follow that methodology to correlate the electrochemical results to the differences in the physical parameters obtained for each technique.

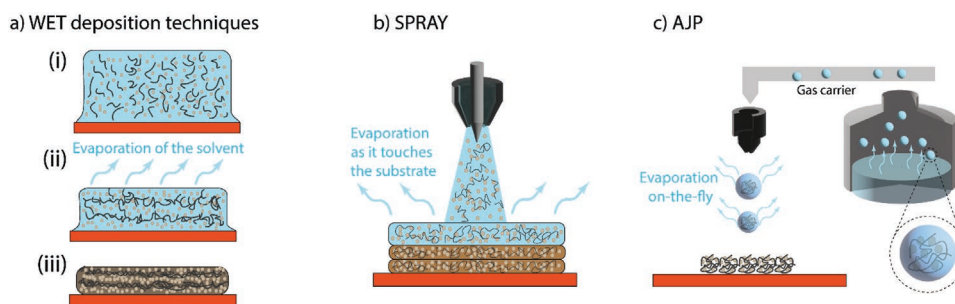
We start defining the magnitude “rate” as shown in Equation (1), being I_M current per mass and Q_M the experimental specific capacity.

$$R = I_M / Q_M \quad (1)$$

This magnitude has the advantage to relate directly to the experimental charge/discharge time of the cell by $\approx 1/R$.^[10] The semiempirical equation we use to describe the specific capacity as a function of the rate is shown in Equation (2), where Q_{M0} is the low rate specific capacity, τ the characteristic time, and n the slope behavior.^[10]

$$Q_M = Q_{M0} \left[1 - (R \cdot \tau)^n \cdot \left(1 - e^{-(R \cdot \tau)^n} \right) \right] \quad (2)$$

The physical meaning of τ is the characteristic time associated with the charge/discharge. It is a measure of the minimum time required to fully charge the device, **Figure 2a**, and the point at which the capacity starts to fall with the rate.^[18] The exponent n describes the decay behavior at a high rate and indicates the rate-limiting mechanism of the cell. Its values are generally comprised between 0.5 and 1, which corresponds to diffusive and resistive limitations respectively.^[18]



Scheme 1. a) Scheme of the drying process of the wet deposition techniques, i.e., slurry casting, filtration, and extrusion (DIW). i) After the deposition of the ink, ii) the solvent starts to evaporate, iii) forcing the dispersion to crash and catalyzing the segregation and agglomeration of the CNTs and LTO. iii) Once the material is dried the end layer shows high segregation in its microstructure. b) Representation of the deposition and drying process of the spray coating technique. Layers are deposited in wet but very thin coats, allowing a reduced material rearrangement capability. Networks are present but are generally thin and widespread. c) Scheme of AJP deposition process. To avoid coffee ring effects and improve adhesion, the droplets reach the substrate with minimal content of solvent that evaporates quickly after deposition.^[16] This method produces films with very little self-rearranging capabilities and produces a microstructure completely different to those of the wet techniques.

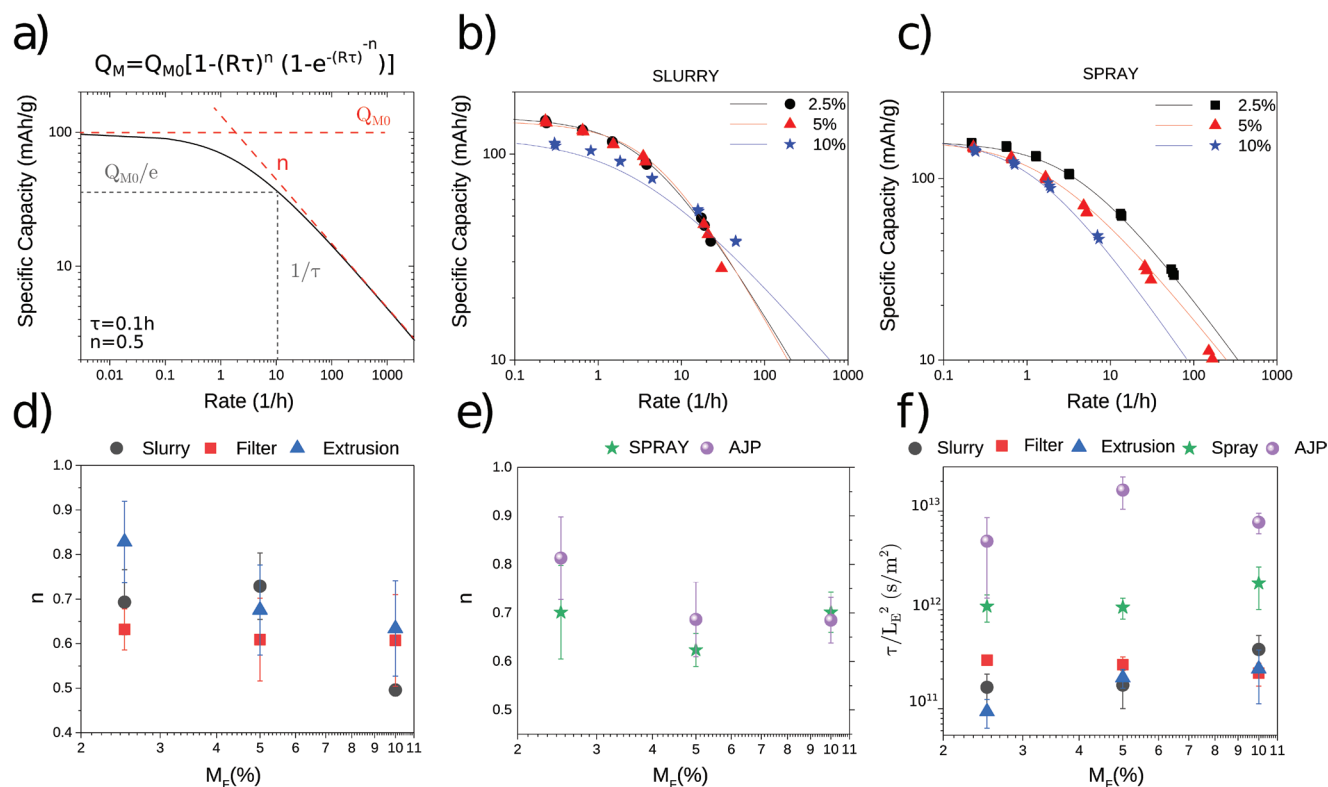


Figure 2. a) Brief description of the effect of each parameter used in the semi-empirical model discussed in Equation (2). The parameters used for the plot are shown in the inset. Adapted from reference [10]. b) Specific capacity versus the rate of representative slurry and spray c) electrodes with the indicated CNT M_F . Solid lines correspond to CA tests while the symbols to GC. Similar plots for the other techniques can be found in Figure S7 (Supporting Information). d) Exponent “ n ” versus the CNT M_F for e) “wet” and “dry” techniques. f) Characteristic time divided by the square of the electrode thickness (τ/L_e^2) against the CNT M_F for all the techniques. The displayed values of the fitting parameters are obtained from averaging the data from CA and GC test of sets of samples from 3 to 7 cells. The errors displayed correspond to the standard deviation of each set.

Using this model we can fit our rate-dependent capacity tests to extract Q_{M0} , τ and n . This method is a powerful tool for the quantitative analysis of batteries, as it allows for building up statistics and a much more methodical analysis of the rate-dependent tests.

We analyzed cells corresponding to the five techniques and three CNTs mass fractions both by GC and CA. Results are displayed in Figure 2b,c and Figure S7 (Supporting Information). It is worth mentioning that GC tests, represented in the graphs by symbols, were initially launched in terms of C-Rate and then changed to rate following Equation (1). For that reason, the position of the GC data is not always displayed in the same position respective to the X-axis. The representation and transformation of the current transients from the CA into the capacity-rate data shown in the figures are further explained in the Supporting Methods section and references.^[17,19]

For each CNT M_F corresponding to each technique, we analyzed and fitted the data of sets containing between 3 to 7 cells by CA and GC. The results obtained for the Q_{M0} are displayed in Figure S8 (Supporting Information), while the averaged values of n are shown in Figure 2d,e. For most techniques, it is observed that the increase of the CNT M_F catalyzes a change in the rate-limiting behavior (n), from resistive limited at low M_F to a more diffusion-limited at high M_F , which agrees with previous reports.^[10] This change is sharper in the electrodes produced by wet techniques, while for those fabricated by dry techniques,

their n values seem to saturate at 0.7 even at high CNT M_F . The reduction of the slope in the high rate region (lower n) implies better capacity retention that seems to improve the more CNTs are present in the sample, although samples with segregated networks seem to experience a more substantial change.

Surprisingly, some techniques do not show major changes in their behavior regardless of the M_F , i.e., filtration and spray. The reason behind this observation might be that they achieved their saturation value outside the CNT M_F studied, as the change in rate-limiting behavior seems rather abrupt.^[10] It is also worth mentioning that the thickness of the electrodes does not seem to affect significantly the exponent n , Figure S9 (Supporting Information), at least within the mass loadings studied. This is quite interesting as if the rate-limiting behavior was directly related to the resistance inside the electrode, as the dependence with the conductive additive suggests, the thickness of the electrodes should trigger the change of behavior. This, and the fact that the network arrangement affects so substantially the n value, suggest that the change of behaviour might be related to a balance between the electronic conductivity and the diffusion of the ions along the porous structure of the electrode, as these are the main values that are altered across techniques.

Although n can give us some information about the structural/compositional parameters that influence the performance of our batteries, the characteristic time τ , has been far more studied for this purpose and its correlation with specific

battery parameters has been clearly described.^[10,18,20] We can understand τ as an RC circuit time constant with three major terms, one from the electrical and ionic resistances of the electrode and separator, another associated with the mass transfer, including the diffusion of ions in the electrolyte through the pores of the electrode and separator and the solid diffusion of the ions in the material, and finally one term associated with the timescale of the electrochemical reaction, Equation (3).^[10] This relationship can be further developed and rewritten as shown by Equation (4).^[10,20]

$$\tau = \tau_{\text{Electrical}} + \tau_{\text{Diffusion}} + t_c \quad (3)$$

$$\tau = L_E^2 \left[\frac{C_{V,\text{eff}}}{2\sigma_{\text{OOP,E}}} + \frac{C_{V,\text{eff}}}{2\sigma_{\text{BL}}P_E^{3/2}} + \frac{1}{D_{\text{BL}}P_E^{3/2}} \right] + L_E \left[\frac{L_S C_{V,\text{eff}}}{\sigma_{\text{BL}}P_S^{3/2}} \right] + \left[\frac{L_S^2}{D_{\text{BL}}P_S^{3/2}} + \frac{L_{\text{AM}}^2}{D_{\text{AM}}} + t_c \right] \quad (4)$$

To compare the different deposition techniques and CNTs M_F , we can simplify Equation (4) into Equation (5) by considering constant the terms associated with the processes that are not altered by those changes. Those are the ones related to the separator (terms 4 and 5), the solid diffusion of ions (term 6) and the electrochemical reaction (term 7).

$$\tau = L_E^2 \left[\frac{C_{V,\text{eff}}}{2\sigma_{\text{OOP,E}}} + \frac{C_{V,\text{eff}}}{2\sigma_{\text{BL}}P_E^{3/2}} + \frac{1}{D_{\text{BL}}P_E^{3/2}} \right] + L_E b + c \quad (5)$$

This gives us an expression that only depends on the thickness (L_E), porosity (P_E), out-of-plane conductivity ($\sigma_{\text{OOP,E}}$) and effective volumetric capacitance of the electrodes ($C_{V,\text{eff}}$), with ion diffusion and ion conductivity (D_{BL} and σ_{BL} respectively) being constant across our samples. All these parameters are in the term accompanying L_E^2 in Equation (5); therefore, to compare the different techniques is more convenient to use τ/L_E^2 rather than τ , as the other terms will not change significantly. Indeed, τ/L_E^2 has been proposed in the literature as a figure of merit for the comparison of battery materials.^[10,21] Additionally, if we study the dependence of τ with the electrode thickness, Figure S10 (Supporting Information), we obtain a second-order polynomial with a parameter “a” (the one accompanying L_E^2) which is much more relevant to the studied thicknesses than any of the other parameters. This value, as well as the ratio between “a” and “b,” agrees well with the observed by Tian et al. for a large set of battery electrodes from the literature.^[10]

If we observe the values of τ/L_E^2 for the different techniques and CNT M_F s, in Figure 2f, we note very significant differences across the deposition methods. Quite interestingly, all the techniques that we classified as “wet” due to their drying behavior and the arrangement of their conductive matrix in the form of segregated networks, show a very similar τ/L_E^2 . Conversely, Spray and AJP samples, that we classified as “dry,” show much higher values, and therefore worse rate performance, than those of the wet techniques, being an order of magnitude higher for spray and two orders of magnitude for AJP. It is important to emphasize the importance of these results, as they imply that samples produced by spray and AJP will see a very significant drop in their rate performance compared to the wet techniques.

It also highlights the tremendous importance that the material arrangement can have in an electrode.

The CNT M_F has very little influence on the τ/L_E^2 , regardless of the deposition technique; or at least this is the case for the M_F explored.

To further understand the abrupt changes observed in the characteristic times between techniques, we can refer to Equation (5). We can use this relationship to identify the physical parameter that limits τ , and thanks to the assumptions described above, we can narrow the suspects to the porosity of the electrodes, their conductivity and volumetric capacitance.

2.3.1. Effect of the Porosity on the Rate Performance

We measured the porosity of the electrodes, as per described in the Methods section, for all the samples produced by every technique and CNT M_F , Figure 3a. Again, we observe very dissimilar behavior when we compare wet and dry techniques. All the wet techniques show similar porosity values and follow the same trend, with increasing porosity with the amount of CNTs. Conversely, the dry techniques show a stable porosity that does not depend upon the ratio of CNTs/LTO. Interestingly, porosity seems to depend on the technique itself, as spray and AJP show very different values. These results are further supported by the gas adsorption analysis, Figure 3c, which shows the same trends as those of the apparent porosity. In fact, these results highlight better the differences between wet and dry techniques as they account better for the microstructure of the electrodes without considering very large macroporous channels.^[22]

The reason behind the steady increase of the porosity with the CNT content for the wet techniques may be attributed to the formation of segregated networks. As we add more CNTs, these incorporate into the networks rather than in between the LTO, creating two regions, one with almost the same porosity as the pure LTO and one with that of the CNT films. The bigger the CNT proportion, the thicker the segregated networks get and the closer they get to the values of the pure CNT film as shown in Figure S12 (Supporting Information). The pore size volume distribution also follow this trend, Table S1 and Figure S14 (Supporting Information). In the case of the dry techniques, since the CNTs are more homogeneously distributed with the LTO, the changes induced by the increase of M_F are smaller and the intrinsic porosity created by the technique governs the overall porosity. In fact, in macroporous materials, the increase of the CNT M_F can even reduce the porosity, as they can fill the pre-existing pores.^[23] This could explain why in Figure 3c, the spray and AJP samples see their pore volume reduced when the CNT content is increased from 2.5% to 10% and also why the pore size volume distribution changes at high CNT ratio in the dry techniques, Figure S14 (Supporting Information).

We can explore the influence of the porosity on the rate performance through the τ/L_E^2 , by plotting these two parameters against each other, as shown in Figure 3b and Figure S15 (Supporting Information). We can easily observe that the values do not show any clear correlation across the techniques. In fact, the relationship that these two parameters should follow (dashed line in Figure 3b corresponding to Equation (S7), Supporting Information) cannot explain the distribution of the data across

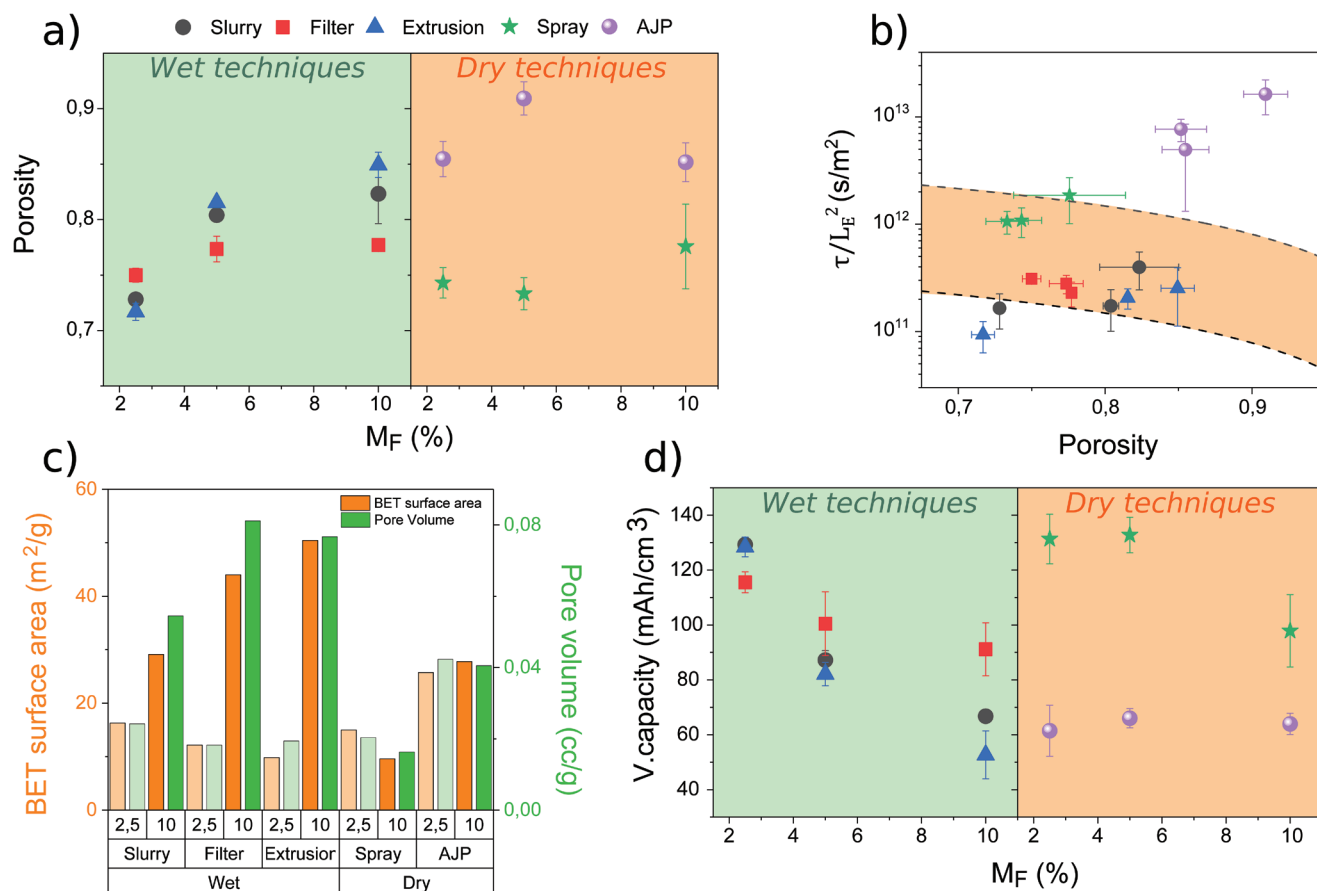


Figure 3. a) Apparent porosity versus the CNT M_F . Wet techniques are displayed on the left side (green background) and dry techniques on the right (orange background). b) Characteristic time divided by electrode thickness squared (τ/L_E^2) against the apparent porosity. The graph shares the legend with graph (a). The dashed lines represent the relationship between τ/L_E^2 and porosity according to Equation (S7) (Supporting Information) with the parameters described in the Supporting Methods. The two dashed lines represent the most dissimilar parameters of the electrodes we produced, while the orange area between them, intermediate fabrication parameters. c) BET surface area and Pore volume for the selected techniques and CNT M_F . Wet techniques are on the left side of the plot and dry on the right. The data were obtained from the isotherms in Figure S11 (Supporting Information). d) Volumetric capacities versus CNT M_F for all techniques; the legend is shared with (a).

techniques. However, it can explain quite well the behavior of the data corresponding to the “wet” techniques. This means that although porosity is a parameter difficult to simulate through a model due to its influence in other magnitudes such as conductivity or internal resistances,^[24–26] all the other parameters change so little within the “wet” techniques that the samples adhere very well to the dependency with the porosity. This clearly shows that despite porosity is not the main factor responsible for the difference between the rate performance of the different deposition techniques, it has an important role in the electrodes. We can see that this is indeed true for instance in the volumetric capacity, Figure 3d, where it follows perfectly the reverse trend of the porosity; the more porous the electrode gets, the lower the capacity per unit of volume it has. A similar trend is observed for the pore volume as well, Figure S16 (Supporting Information). It is also interesting to observe the high positive correlation between the porosity and the charge transfer resistance of the electrodes, Figure S17 (Supporting Information), which shows similar behavior as in other systems.^[26,27] Although it is important to mention that this magnitude is also affected by other parameters such as the volume fraction of the

additives, that change along with the CNT content, so it can be a combination of effects^[25,28] that would require a more detailed analysis to precisely correlate.

In common battery electrodes, porosity is a parameter that can be easily adjusted by calendaring the composites, but as we move to more advanced manufacturing techniques and designs, this option no longer becomes available and is something to carefully consider when selecting our fabrication technique.

2.3.2. Effect of the Conductivity in the Rate Performance

We measured the in-plane (IP) and out-of-plane (OOP) conductivity of the electrodes as described in the Supporting Methods. For the OOP we used a two-probe approach, which, includes the effect of the contact resistance.^[20] Although this value is non-trivial, we can isolate our electrode resistance by measuring samples with the same contact areas and composition but changing their thicknesses, Figure S19 (Supporting Information). Comparing these values with those obtained by direct probing, we can see that the difference between them falls

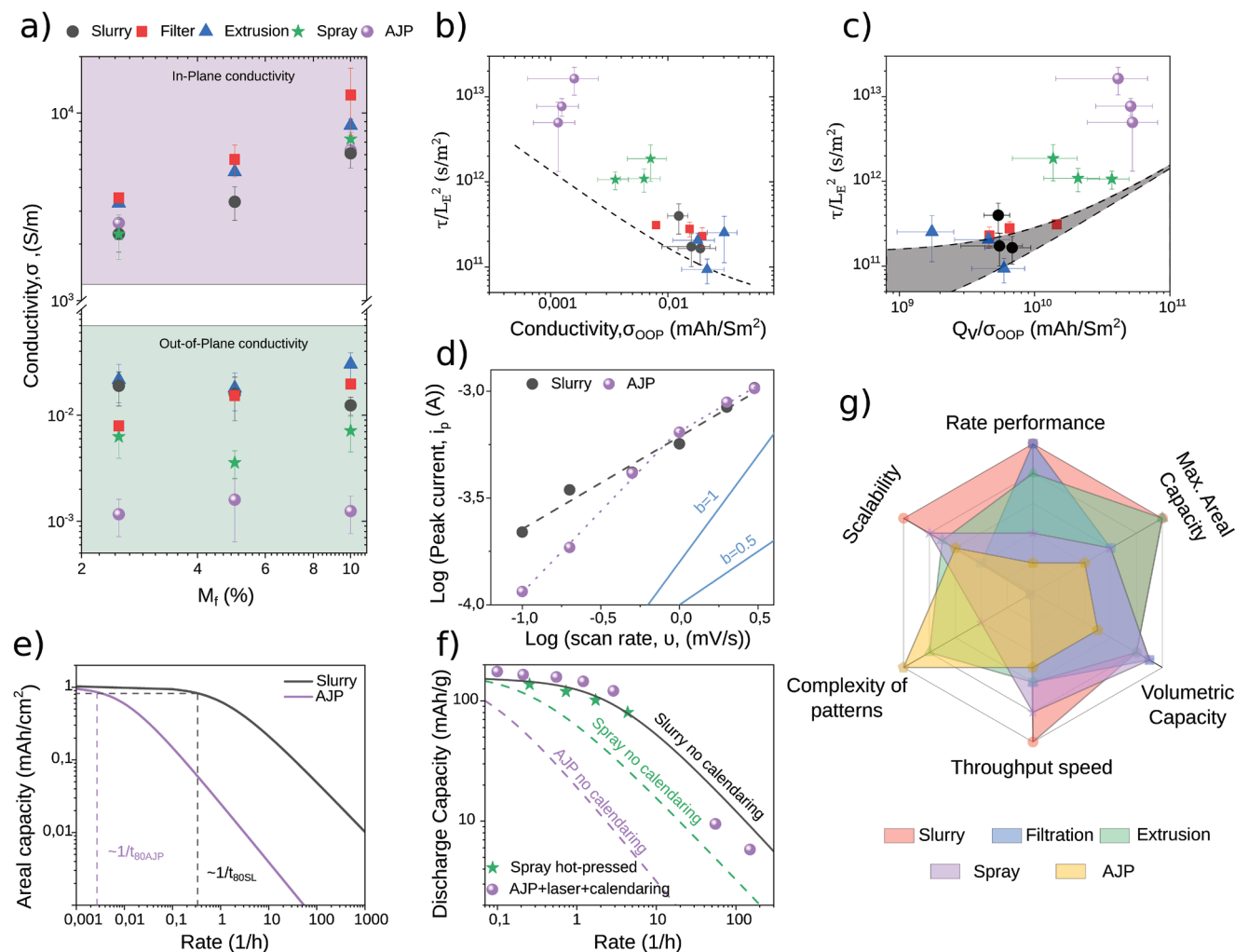


Figure 4. a) In-plane (purple background) and out-of-plane (blue-green background) conductivities for different CNT M_f and techniques. The in-plane conductivity was measured by 4-point probe while the out-of-plane conductivity was measured as described in the supportive information. b) Characteristic time divided by electrode thickness squared (τ/L_E^2) plotted against the out-of-plane conductivities. The gray dashed line corresponds to the representation of Equation (5) rearranged in the shape of Equation (S7) (Supporting Information) using the parameters shown in Supporting Methods. c) τ/L_E^2 plotted versus the volumetric capacity divided by the out-of-plane conductivity (Q_V/σ_{OOP}). The two dashed lines that enclose the gray area, represent Equation (6) with the parameters described in Supporting Methods and correspond to the experimental limits among which our electrodes are usually found. d) Plot of the peak current vs scan rate of the slurry and AJP samples to obtain the b -value according to $i_p = av^b$. The CVs from which the peak values were obtained are displayed in Figure S20 (Supporting Information). e) Simulated areal capacity plotted versus rate for slurry and AJP electrodes considering the necessary thickness to achieve the same areal capacity considering the values shown in Figures 2 and 3. f) Comparison of literature results for spray and AJP samples with 5% conductive additive and post-synthetic treatments,^[29,30] with our slurry, spray, and AJP samples with 2.5% CNT content and no calendering. Literature data are represented with symbols while our data with lines. The solid lines indicate experimental data from a cell, while the dashed lines simulated curves using the experimental parameters obtained. All samples, including the literature data, have the same thickness (60 μm). g) Qualitative radar map of the techniques explored in this work attending to the five categories displayed in the map. The score assigned to the categories “Rate performance,” “Max. Areal Capacity,” and “Volumetric Capacity” are based on the results obtained in this work, while the other scores were adapted from references.^[31]

within the statistical error across samples, and therefore we can consider the contact resistance small enough to not be considered for the OOP measurements.

The IP and OOP conductivities are displayed in Figure 4a. All techniques yield similar results for the IP conductivity showing the same trend with the CNT M_f regardless of the technique. Conversely, the OOP conductivities show very different results across techniques and seem to be quite insensitive to the change of CNT M_f . The explanation for the latter could be that

the statistical error is clouding the changes of this magnitude, or simply that the M_f we are working with are far enough from the percolation threshold, and therefore reaching the saturation value.^[20] Regarding the changes in OOP conductivity with the deposition techniques, again, we observe differences over an order of magnitude between the “wet” and “dry” techniques. All “wet” techniques display very similar values that match those of segregated networks in the literature,^[20] while spray and AJP parameters are significantly lower. Interestingly, these

differences are similar to those obtained when comparing segregated CNT networks to other conductive additives that don't form these structures.^[8,20]

The OOP conductivity results in Figure 4a resemble those obtained for the τ/L_E^2 , and indeed, if we plot it against $\sigma_{\text{OOP,E}}$ (Figure 4b) we can see that there is a clear correlation between them. Furthermore, if we compare the experimental points with the representation of Equation (5) (dashed line in Figure 4b using the parameters indicated in the Supporting Methods), we observe that the data follow very accurately the same dependence with the $\sigma_{\text{OOP,E}}$. This implies that OOP conductivity is indeed the limiting factor of the rate performance and its changes across techniques explain the differences we observed in the characteristic times. It also infers that the samples are limited by the part of the RC charging time associated with electrode resistance.

The deposition technique, therefore, affects the microstructure of the electrode, which, in turn, changes the OOP conductivity of the composite. The characteristic time, which is what we consider as "rate performance," is therefore mainly dictated by the OOP conductivity as shown in Figure 4b. The OOP conductivity in this material is therefore the parameter that needs to be optimized and the one that changes the most across deposition techniques.

2.3.3. Volumetric Capacitance and Rate Performance

Going back to Equation (5)'s first term, we can observe that together with $\sigma_{\text{OOP,E}}$ we also have a contribution from $C_{\text{V,eff}}$. Since we have just demonstrated that this first term is the one that dominates over τ/L_E^2 thanks to the $\sigma_{\text{OOP,E}}$, it is interesting to explore which role $C_{\text{V,eff}}$ might play.

Tian et al. proposed that the volumetric capacitance, $C_{\text{V,eff}}$, in battery electrodes is related to the volumetric capacity, Q_V , by the following relationship: $\frac{C_{\text{V,eff}}}{Q_V} = 28 \text{ F mAh}^{-1}$.^[10] Since we already obtained the Q_V of our electrodes (Figure 3d), we can use it to plot τ/L_E^2 versus the $Q_V/\sigma_{\text{OOP,E}}$ (Figure 4c). By combining the first term of Equation (5) and the relationship between $C_{\text{V,eff}}$ and Q_V , we can therefore obtain Equation (6).

$$\frac{\tau}{L_E^2} = 14 \frac{Q_V}{\sigma_{\text{OOP,E}}} + \frac{B}{L_E^2} \quad (6)$$

If this equation applies to our electrodes, the data in Figure 4c should align relatively well with a grade 1 polynomial with slope 14 and an intercept value that will depend on the physical parameters of our cell, B . This is represented in Figure 4c as a gray area, which is the area delimited by Equation (6) using as intercept the most extreme fabrication values we used and which are described in detail in the Supporting Methods. While the wet techniques align well with this relationship, the dry ones do not. This observation is very interesting as it implies that the relationship between $C_{\text{V,eff}}$ and Q_V might change depending on the physical parameters of the electrodes. This observation is further supported by the evaluation of the b -values from the plot of the peak current vs scan rate through the relationship $i_p = a\nu^b$, Figure 4d. Here, we can see that the AJP sample has a contribution from a non-diffusion limited

current that contrasts with the slurry sample that is instead diffusion-controlled for the whole scan rate range. Although the results extracted from the current peaks in the CV are merely qualitative,^[32] these two hints might indicate a difference in their $C_{\text{V,eff}}$ to Q_V relationship. The origin of this difference between electrodes is unclear, however, the higher roughness of the AJP samples (Figure S5, Supporting Information), and a higher volume of open micro-pores, Table S1 (Supporting Information), could be contributing to it.

2.4. Prediction of Performance and Comparison of Techniques

Following the methodology described in the previous section, we were able to examine the differences between the five deposition techniques and correlate the changes in their electrochemical performance to changes in their physical parameters such as porosity and material arrangement. Using the fitting parameters obtained (Figure 2) in combination with the volumetric capacitances (Figure 3d) we can predict the response of the electrodes fabricated by different techniques. This is extremely useful in terms of device engineering and as a way to select the appropriate technique for the requirements of the device. For instance, we can consider the most dissimilar techniques, i.e., Slurry casting and AJP, and predict how they will perform under the same fabrication parameters. If we consider films produced by these techniques with an equal areal capacity of 1 mAh cm^{-2} , using for their parameters those shown in Figure 2 (their " n " and τ) and Figure 3 (their volumetric capacity), we can obtain their rate-dependent response, Figure 4e. To compare their performance more easily, we can calculate the rate at which their capacity falls to 80% of the low-rate capacity through Equation (7), obtained from Equation (2) taking the low-rate limit where the exponential is negligible.

$$R_{80} = (1/5)^{1/n} / \tau \quad (7)$$

These rates can be interpreted as the reverse of the time that it takes to charge/discharge the battery ($R \approx 1/t_{\text{C/D}}$). Therefore, for the batteries in Figure 4e, the minimum charge/discharge time at which we retain 80% of the nominal capacity, is $t_{80 \text{ SL}} = 3 \text{ h}$ for slurry and $t_{80 \text{ AJP}} = 360 \text{ h}$ for AJP.

These large differences in charge/discharge times highlight the importance that the deposition technique can play, and how critical the changes in the associated electrode's microstructure can be in the device's performance.

At this point, it is worth highlighting that for this study we did not compress any of the films produced; this is usually done to reduce the porosity of the films, increase volumetric capacity and improve conductivity, as shown in Figure S21 (Supporting Information). This was done on purpose, to simulate as accurately as possible the conditions that printed structures would generally have, as their compression would not be feasible in practical devices. It is also important to mention that we specifically worked with spray and AJP in the regimes in which the pooling of the material is minimized and therefore patterning becomes easier without further steps. For instance, other authors produced thick samples by AJP with a much more profuse ink stream, subsequently dried with a laser in a second

step.^[30] These films were also compressed afterward obtaining a performance that is closer to our “wet” techniques Figure 4f. Similarly, spray-coated samples with a post-deposition hot pressing treatment produced samples with very good rate performance that also align well with our results (Figure 4f).^[29] These, and other post-synthetic treatments can help to boost the performance of additive manufacturing techniques but are not always compatible with the structures and devices that are meant to conform. In this regard, it is important to highlight that smart patterning and the extra functionalities that the printed devices have, such as flexibility^[33] or miniaturization,^[14] can help to compensate and overcome their intrinsic lower performance.^[31,34] For instance, while AJP can create patterns as thin as 10 μm with high aspect ratios,^[35] the patterning capabilities of slurry or filtering techniques are very limited. It is important to consider this and other capabilities along with performance, as the ideality of a technique for a specific application is based on numerous factors. In this regard, Figure 4g shows a qualitative snapshot of some of the parameters that are generally considered important in the engineering of energy storage devices and allows a quick assessment of the appropriateness of a technique for certain objectives. This radar map highlights for example the versatility of extrusion printing, the lack of scalability of vacuum filtration or the inability of the slurry casting to create complex structures. We have contributed to completing this map of properties by fully characterizing the performance drops that occur when different techniques are applied, and we have been able to identify the root of these changes through a mechanistic model. These results are therefore very useful when selecting a technique and optimization strategies.

3. Conclusions

We have fabricated LTO/CNTs composite battery electrodes by five different deposition techniques including slurry casting, vacuum filtration, 3D extrusion printing, AJP and spray coating. We analyzed their microstructure observing clear differences depending on the drying mechanism and time, being able to categorize the techniques into two broad groups we named “wet” and “dry,” the first showing the presence of CNTs segregated networks while the latter a non-preferential distribution. The changes in the microstructure were observed to alter very significantly the rate performance of the electrodes, and using a semi-empirical equation to fit the data in combination with a mechanistic analysis of their parameters, we were able to find the root of the differences across techniques. By plotting τ/L_E^2 versus different magnitudes, we identified that the OOP conductivity was the limiting factor in the rate performance of our electrodes although porosity also plays an important role too. Interestingly, worse conductivities and therefore characteristic times were obtained for those techniques that didn't show segregated networks, i.e., those catalogued as dry techniques.

We used the results obtained in this work to complete the picture of the printing/additive manufacturing techniques, benchmarking their performance and taking into account other important design parameters. Our results highlight the importance of the microstructure on the battery electrodes and how deposition techniques influence over it. This understanding is

a key point in the optimization of the devices as it allows for the design of specific routes to overcome their limitations. For instance, the minimum gain in performance that the increase of CNT content brings to the “wet” techniques is counterbalanced by a substantial increase in porosity and therefore lower volumetric capacity. This makes the lowest concentration of CNTs the most optimal ink for these techniques. Additionally, the use of post-synthetic treatments can help to bring the performance of the samples with no segregated networks close to the ones with them, although these treatments are not always compatible with the device architecture, especially in miniaturized devices. AJP's lower performance can be compensated with smart patterning, thin layering and its inherent capability to deposit material over pre-patterned substrates, aiming to reduce the effective thickness of the films while maintaining high mass loading, i.e., artificially creating a layer of conductive additive in between layers of active material or pre-patterning conductive pillar or walls in the substrate prior the active material deposition.

These are only a few examples of optimization strategies that can be designed based on the results of this article but many more will be surely suggested by the 3D printing and battery community.

4. Experimental Section

Material Characterization: The crystal structure of the samples at different stages of the processing was studied by X-ray diffraction (XRD) (D5000 powder diffractometer, Bruker, USA) with a monochromatic Cu K radiation source ($\lambda = 0.15406 \text{ nm}$) and a secondary monochromator. The scanning electron microscopy (SEM) was performed with a Zeiss Ultra Plus (Carl Zeiss, Germany) equipment with a built-in EDS capabilities. The transmission electron microscopy was done with a FEI Titan high-resolution TEM (HRTEM) at 300 kV (FEI, USA), using as substrates for the samples holey carbon grids (Agar Scientific, UK).

LTO/CNT Ink Preparation: Raw $\text{Li}_4\text{Ti}_5\text{O}_{12}$ powders were purchased from Linyi Gelon LIB Co and single-wall carbon nanotubes were purchased in solution (0.2% in weight and 0.3% CMC as a stabilizer in water) from OCSiAl. The inks were prepared in 2.5%, 5%, and 10% CNTs M_F with an approximate solid content of 5%. Large (25 mL) batches were prepared to feed simultaneously all the techniques, for which the LTO was added in powder to a centrifuge tube followed by a few droplets of IPA to make it into a dense paste. Afterward, water-based CNTs dispersions were added to the tube until the desired proportion was obtained. Mixtures were vigorously stirred with a vortex mixer (Fisherbrand) followed by a 10 min sonication in a sonic bath (Fisherbrand, 37 kHz) and a final stirring step in the mixer.

Electrodes Preparation: All electrodes were prepared using a Cu foil (9 μm , MTI Corp, USA) as current collector. A wide variety of active material thicknesses were prepared ranging from 10 to 100 μm . Slurry cast electrodes were prepared by direct application of the as-prepared inks on the Cu foils with a Micrometer Adjustable Doctor Blade (MTI Corp, USA). The vacuum-filtrated electrodes were prepared by mixing the active material (LTO), Tuball CNTs and water together by magnetic stirring for 15 min. Subsequently, the mixture was placed in a sonic bath (FisherBrand 11207) for 5 min at frequency of 37 Hz. The mixture was then filtered by vacuum filtration (EMD Millipore 47 mm Glass Vacuum Filter) using the electrochemical cell separator (polyolefin) as filter paper and was left to dry for several hours. The dried composite was then removed from the filter forming a free-standing film and electrodes were cut. For the 2.5% composite electrodes, Cellulose Nitrate Membranes (Whatmann, 0.2 μm) were used as filter paper and subsequently dissolved using acetone to form a freestanding electrode.

The extrusion-printed electrodes were fabricated using a Nano3Dprint (Burlingame, CA, USA) dual extrusion printer. As prepared inks were loaded into standard 3.5 mL syringes with 22 Ga syringe nozzles with a 0.40 mm inner nozzle diameter. The print platen was heated to 70 °C. Print speed was ranged between 600 and 1800 mm min⁻¹. Extrusion was normalized with respect to print speed so mass deposited remains equal for each layer regardless of print speed. This was to promote adhesion of the first layer through drying. Distance between the nozzle tip and the substrate was kept constant to ensure a connected liquid flow between the nozzle and substrate. The spray-coated electrodes were prepared using a Harder and Steenbeck Infinity Airbrush attached to a Janome JR2300N mobile gantry with a substrate temperature of 70 °C. As carrier gas, N₂ was used with a back pressure of 25 psi and a nozzle diameter of 0.4 mm. The spraying distance was 100 mm and inks were pre-diluted to a concentration of 10 mg mL⁻¹ just before the spraying. The aerosol jet printed samples were printed using an Optomec AJP 300 (Optomec Inc, Albuquerque, NM, USA) aerosol jet printer. Deionized water was used to dilute the as prepared inks for aerosol jet printing in a 2:1 ratio. The pneumatic atomizer attachment of the printer was used to generate the high volume of aerosol required for large-area electrodes, using an N₂ carrier gas for both pneumatic aerosolizing and nozzle focusing. Stand off distance between nozzle tip and substrate was set at 5 mm, with a process speed of 10 mm s⁻¹. The print plate was set to 70° for the duration of the print. Regardless of the preparation method, the samples were subsequently subjected to a 2-h thermal treatment of 400 °C at low pressure and under Ar flow to remove the CMC. TGA of the CNTs with the CMC, Figure S19 (Supporting Information), indeed shows that this treatment is sufficient to remove the CMC.

Batteries Assembly: All the batteries were assembled in half-cell configuration using 2032-type coin cells (MTI Corp). The working electrodes were punched with $d = 1.2$ cm and tested against a Li reference/counter electrode ($d = 1.5$ cm, MTI Corp, USA) using a Celgard 2320 separator and LP30 (1M LiPF₆ in EC/DMC, 1:1 in v/v, BASF) as electrolyte. Cells were assembled in an Ar-filled glovebox (UNIlab Pro, Mbraun) with O₂ and H₂O levels < 0.1 ppm.

Electrochemical Testing: The galvanostatic tests were measured in an ARBIN LBT21084 using a symmetric charge/discharge protocol with C-rates ranging between 0.2 C up to 10 C and using 1.2–2.4 V as the voltage range. The chronoamperometry tests were also performed with an ARBIN LBT21084. Cells were galvanostatically cycled for 5 cycles at 0.1 C before they were charged up to the upper voltage at 0.1 C and then the CA took place at the lower cut-off potential. The cyclic voltammetric and potentiostatic electrochemical impedance spectroscopy tests were performed in a VMP3 potentiostat (Biologic). PEIS data was obtained using a frequency range between 50 kHz and 50 mHz with 6 points per decade. The impedance spectroscopy data was analyzed with a python script using “impedance.py” package.^[36]

BET Measurements: To assess the porosity and the surface area of the samples, nitrogen adsorption at 77 K was measured using a Quantachrome Autosorb-IQ. Prior to the measurements, each sample (± 10 –20 mg) has been activated overnight at 150 °C under a secondary vacuum. In a typical experiment, adsorption curves have been measured in the range of 0.0001–0.99 p/p₀, and desorption curves in the range of 0.99–0.3 p/p₀.

To determine the pore volume, the Gurvich rule at 0.95 p/p₀ was used. This method assumes that the pressure is high enough so the nitrogen in the pores is actually in a bulk liquid state. Limiting the value at 0.95 is also used to avoid considering macropores and inter-particle voids.

To determine the surface area, the classic BET method was used.^[37] This method consists in the linearization of the isotherm into a “BET plot” which allows the determination of the nitrogen monolayer adsorption capacity of the samples. Knowing the cross-sectional surface of adsorbed N₂ molecules (0.162 nm²), the BET surface area of the sample can be determined.

To determine the Pore Size Distribution of the Carbon NanoTubes, the DFT method provided in the Quantachrome ASiQwin software was used. The model used is “N₂ at 77 K on carbon (cylindr.pores, NLDFT equilibrium model).”

In-Plane Conductivity Measurements: Conductivity measurements were performed with a 4-point probing device (Signatone SYS-310, California, USA), a Keithley 2400 (Keithley Instruments, Ohio, USA) as source meter and a 4-point probe head (Signatone SP4, California, USA) with 1016 μ m tip spacing and 45 g of pressure. Samples areas were above 1 cm² and were tested at room temperature.

Supporting Information

Supporting Information is available from the Wiley Online Library or from the author.

Acknowledgements

The authors acknowledge financial support from the European Union’s Horizon 2020 research and innovation programme under the Marie Skłodowska-Curie Grant Agreement No. 713567, European Union’s Horizon 2020 research and innovation programme and the Iberdrola Foundation under the Marie Skłodowska-Curie Grant Agreement No 101034297, and Science Foundation Ireland Research Centre award 12/RC/2278_P2. S.R. wishes to thank the Irish Research Council (GOIPG/2019/2428) for funding a PhD studentship.

Open access funding provided by IReL.

Conflict of Interest

The authors declare no conflict of interest.

Data Availability Statement

The data that support the findings of this study are available from the corresponding author upon reasonable request.

Keywords

additive manufacturing, energy storage devices, Li-ion batteries, LTO

Received: November 4, 2022

Revised: February 1, 2023

Published online: March 2, 2023

- [1] X. Tian, J. Jin, S. Yuan, C. K. Chua, S. B. Tor, K. Zhou, *Adv. Energy Mater.* **2017**, 7, 1700127.
- [2] 3D Printing Market Size, Share & COVID-19 Impact Analysis. F.B.Insights, **2022**, FB1101902.
- [3] Z. Lyu, G. J. H. Lim, J. J. Koh, Y. Li, Y. Ma, J. Ding, J. Wang, Z. Hu, J. Wang, W. Chen, Y. Chen, *Joule* **2021**, 5, 89.
- [4] Sakuu Achieves New Battery Benchmark of 800 Wh/L Energy for Wide Industry Applications | Sakuu | Sakuu, can be found under <https://sakuu.com/> (accessed: September 2022).
- [5] The basis of the implementation of 3-D printed sodium-ion batteries will be ready for the market by 2025 Blackstone Resources AG, **2022**.
- [6] B. Elder, R. Neupane, E. Tokita, U. Ghosh, S. Hales, Y. L. Kong, *Adv. Mater.* **2020**, 32, 1907142.
- [7] K. Fu, Y. Yao, J. Dai, L. Hu, *Adv. Mater.* **2017**, 29, 1603486.

- [8] S.-H. H. Park, P. J. King, R. Tian, C. S. Boland, J. Coelho, C. (John) Zhang, P. McBean, N. McEvoy, M. P. Kremer, D. Daly, J. N. Coleman, V. Nicolosi, *Nat. Energy* **2019**, *4*, 560.
- [9] Z. Ling, A. Harvey, D. McAteer, I. J. Godwin, B. Szydłowska, A. Griffin, V. Vega-Mayoral, Y. Song, A. Seral-Ascaso, V. Nicolosi, J. Coleman, *Adv. Energy Mater.* **2018**, *8*, 1702364.
- [10] R. Tian, S.-H. H. Park, P. J. King, G. Cunningham, J. Coelho, V. Nicolosi, J. N. Coleman, *Nat. Commun.* **2019**, *10*, 1933.
- [11] J. Coelho, A. Pokle, S. H. Park, N. McEvoy, N. C. Berner, G. S. Duesberg, V. Nicolosi, *Sci. Rep.* **2017**, *7*, 7614.
- [12] C. J. Zhang, S.-H. Park, O. Ronan, A. Harvey, A. Seral-Ascaso, Z. Lin, N. McEvoy, C. S. Boland, N. C. Berner, G. S. Duesberg, P. Rozier, J. N. Coleman, V. Nicolosi, *Small* **2017**, *13*, 1701677.
- [13] A. Tarancón, V. Esposito, M. Torrell, M. Di Vece, J. S. Son, P. Norby, S. Bag, P. S. Grant, A. Vogelpoth, S. Linnenbrink, M. Brucki, T. Schopphoven, A. Gasser, E. Persembe, D. Koufou, S. Kuhn, R. Ameloot, X. Hou, K. Engelbrecht, C. R. H. Bahl, N. Pryds, J. Wang, C. Tsouris, E. Miramontes, L. Love, C. Lai, X. Sun, M. R. Kærn, G. Criscuolo, D. B. Pedersen, *J. Phys.: Condens. Matter.* **2022**, *4*, 011501.
- [14] J. Zhao, H. Lu, X. Zhao, O. I. Malyi, J. Peng, C. Lu, X. Li, Y. Zhang, Z. Zeng, G. Xing, Y. Tang, *ACS Mater. Lett.* **2020**, *2*, 1041.
- [15] N. Singh, C. Galande, A. Miranda, A. Mathkar, W. Gao, A. L. M. Reddy, A. Vlad, P. M. Ajayan, *Sci. Rep.* **2012**, *2*, 481.
- [16] N. J. Wilkinson, M. A. A. Smith, R. W. Kay, R. A. Harris, *Int. J. Adv. Manuf. Technol.* **2019**, *105*, 4599.
- [17] R. Tian, P. J. King, J. Coelho, S. H. Park, D. V. Horvath, V. Nicolosi, C. O'Dwyer, J. N. Coleman, *J. Power Sources* **2020**, *468*, 228220.
- [18] S. Park, R. Tian, J. Coelho, V. Nicolosi, J. N. Coleman, *Adv. Energy Mater.* **2019**, *9*, 1901359.
- [19] C. Heubner, C. Lämmel, A. Nickol, T. Liebmann, M. Schneider, A. Michaelis, *J. Power Sources* **2018**, *397*, 11.
- [20] R. Tian, N. Alcalá, S. J. O'Neill, D. Horvath, J. Coelho, A. Griffin, Y. Zhang, V. Nicolosi, C. O'Dwyer, J. N. Coleman, *ACS Appl. Energy Mater.* **2020**, *3*, 2966.
- [21] R. Tian, M. Breshears, D. V. Horvath, J. N. Coleman, *ACS Nano* **2020**, *14*, 3129.
- [22] C. Schlumberger, M. Thommes, *Adv. Mater. Interfaces* **2021**, *8*, 2002181.
- [23] T. Nochaiya, A. Chaipanich, *Appl. Surf. Sci.* **2011**, *257*, 1941.
- [24] F. G. Cuevas, J. M. Montes, J. Cintas, P. Urban, *J. Porous Mater.* **2009**, *16*, 675.
- [25] D. Gruet, B. Delobel, D. Sicsic, I. T. Lucas, V. Vivier, *Electrochim. Acta* **2019**, *295*, 787.
- [26] I. Yang, S.-G. Kim, S. H. Kwon, M.-S. Kim, J. C. Jung, *Electrochim. Acta* **2017**, *223*, 21.
- [27] C. W. Tanner, K. Fung, A. V. Virkar, *J. Electrochem. Soc.* **1997**, *144*, 21.
- [28] R. Morasch, J. Keilhofer, H. A. Gasteiger, B. Suthar, *J. Electrochem. Soc.* **2021**, *168*, 080519.
- [29] D. W. Park, N. A. Cañas, N. Wagner, K. A. Friedrich, *J. Power Sources* **2016**, *306*, 758.
- [30] X. Yu, Y. Liu, H. Pham, S. Sarkar, B. Ludwig, I. M. Chen, W. Everhart, J. Park, Y. Wang, H. Pan, *Adv. Mater. Technol.* **2019**, *4*, 1900645.
- [31] S. Pinilla, J. Coelho, K. Li, J. Liu, V. Nicolosi, *Nat. Rev. Mater.* **2022**, *7*, 717.
- [32] A. J. Bard, L. R. Faulkner, *Electrochemical Methods: Fundamentals and Applications*, 2nd ed., John Wiley & Sons, Incorporated, New York **2000**.
- [33] J. Zhao, H. Lu, Y. Zhang, S. Yu, O. I. Malyi, X. Zhao, L. Wang, H. Wang, J. Peng, X. Li, Y. Zhang, S. Chen, H. Pan, G. Xing, C. Lu, Y. Tang, X. Chen, *Sci. Adv.* **2021**, *7*, 6978.
- [34] C. Liu, F. Xu, Y. Liu, J. Ma, P. Liu, D. Wang, C. Lao, Z. Chen, *Electrochim. Acta* **2019**, *314*, 81.
- [35] L. J. Deiner, T. L. Reitz, *Adv. Eng. Mater.* **2017**, *19*, 1600878.
- [36] M. Murbach, B. Gerwe, N. Dawson-Elli, L. Tsui, *JOSS* **2020**, *5*, 2349.
- [37] M. Thommes, K. Kaneko, A. V. Neimark, J. P. Olivier, F. Rodriguez-Reinoso, J. Rouquerol, K. S. W. Sing, *Pure Appl. Chem.* **2015**, *87*, 1051.